Synthetic biosensor circuits with a synchronous precision response to dynamic phytohormone inputs

S. Pérez García[1,†], M. García Navarrete[1,†], D. Ruiz Sanchis[1], C. Prieto Navarro[1], M. Avdovic[1], O. Pucciariello[1], K. Wabnik[1,*]

[1]Centro de Biotecnologıa y Genomica de Plantas (Universidad Politecnica de Madrid – Instituto Nacional de Investigacion y Tecnologıa Agraria y Alimentaria), Autopista M-40, Km 38 – 28223 Pozuelo de Alarcon, Spain

*Correspondence to: k.wabnik@upm.es

†Contributed equally.

Abstract

How dynamic cues (inputs) translate into speed and precision of cell response (output) is one of the most challenging questions in modern biology. Phytohormones auxin and salicylic acid (SA) transfer environmental inputs to signaling pathways that regulate growth and immune responses. There are no direct orthogonal systems capable of detecting phytohormone changes linked to downstream responses in eukaryotes. We created compact synthetic circuits for direct sensing of auxin and SA in yeast by hijacking multiple antibiotic resistance (Mar) proteins from bacteria. By combining all-atom modeling, metadynamics, time-lapse live cell imaging, and bench-top microfluidic technologies we demonstrated that these synthetic circuits detect physiological concentrations of auxin and SA through a dynamic conformational switch of Mar dimer. Synthetic crosstalk of biosensors translates the frequency of hormone inputs into speed, precision, and synchrony of the cell responses in a dynamic environment generated on the microfluidic chip. Our study provides a compact and portable molecular tool that is capable of converting dynamic hormone inputs into clock-synchronized outputs.

Introduction

Among all living matter, plants show remarkable potential for adaption to the environment by maintaining a tight balance between growth and immune responses[1,2]. Phytohormones auxin and salicylic acid (SA) carry information about environmental changes and pass it to complex regulatory networks that tailor plant body architecture[3-8]. This ability to respond to phytohormones was a key innovation in the evolution of plants preceding terrestrial colonization[9]. How dynamic phytohormone cues are translated by individual cells into precisely timed responses is poorly understood.

The quantitative tracking of auxin and SA remains a very challenging task[10-13], largely because existing biosensors for auxin and SA are non-direct, irreversible, and lack a near-linear dynamic range[14, 15]. Development of compact orthogonal phytohormone sensing systems could be instrumental in the understanding of how local changes in phytohormones steer the response dynamics.

A quest for immediate solutions to these problems pointed us to the plant-associated microbes. Several of these microbes control response to environmental stresses by sensing and metabolizing phenol and indole-based compounds reminiscent of plant hormones[16, 17]. Genes derived from such microbes could be used to create minimal biosensing systems aimed in understanding of timing and precision of cell response to transient changes in phytohormones. To explore such possibility, we focused on the family of multiple antibiotic resistance (Mar) proteins that are known for the selective sensing of small aromatic compounds[18, 19]. *E.coli* MarR transcriptional repressor is a representative member of the family that is required for antibiotic stress response (Supplementary Fig.1)[20, 21], however, it is unclear how ligands such as SA regulate MarR repressors activity[19, 20].

Here, we obtain structural insights in phytohormone-dependent regulation of Mar proteins. Next, we constructed compact biosensor circuits for direct sensing of auxin and SA based on putative MarR transcriptional repressors. Minimal synthetic circuits record changes in physiological concentrations of hormones in individual cells with high dynamic range and fidelity. Finally, we demonstrated that a synthetic crosstalk of auxin and SA biosensors realizes various regulatory functions including logic gating as well as synchronization of cell responses to dynamic changes of hormone inputs with tunable speed, precision and memory.

Results

MarR repressors undergo structural transitions from flexible to rigid conformation in the presence of hormones

We initially address the elusive dynamics of ligand sensing by MarR repressors with all-atom molecular dynamics (MD) simulations performed on MarR crystal structures. MD simulations demonstrate that MarR apoprotein remained flexible (Fig. 1a) and adapt to the shape of the DNA operator by adjusting a distance between DNA binding (DB) domains (Fig. 1a and Supplementary Fig. 2a, Supplementary Movies 1 and 2). On the contrary, the presence of SA in the MarR dimerization interface brought monomers close to each other, creating a rigid closed structure (Fig. 1b, Supplementary Movie 3) that was unable to bind DNA. We then calculated the probability distribution of the distance between R73 residues of DB domains that are in direct contact with DNA (Fig. 1c). We found that only apoprotein, largely due to its flexibility (Supplementary Fig. 2b), was able to scan across various distances and eventually sat at the DNA-bound state (Fig. 1c). To address the dynamics of conformation changes, we performed the metadynamics energy landscape analysis with the local perturbation of distance between R73 atoms of both monomers (see SI for details).

Time-dependent changes of energy portraits in apoprotein and DNA-bound MarR configurations revealed the presence of a stable energy minimum (M), which was absent in holoprotein simulations (Fig. 1d). This minimum corresponds to the smallest deviation from the reference distance of ≈ 20 A˚ between DB domains, as observed in crystals of DNA-bound MarR (Supplementary Fig. 2a). Collectively, our findings indicate that MarR repressor requires high flexibility to adapt to DNA operator sites which is negatively regulated by phytohormone exposure.

Several homologs of MarR repressors recognize indole-based compounds[18-21]. Among those, the IacR from *A. Baumanii* is sensitive to naturally occurring auxin such as 3-indoleacetic acid (IAA)[22, 23]. Next, we asked if iacR could respond to auxin using a similar mechanism to that of MarR. The model of iacR predicted that apoprotein remains flexible concerning the spacing between DB domains (Supplementary Fig. 3a). In contrast, the bound IAA stretched the distance between these domains (Supplementary Fig. 3b,c), as demonstrated by the frequency of distance distribution (Supplementary Fig. 4a) and metadynamics analysis

(Supplementary Fig. 4b). Therefore predicted iacR dynamics share common design principles of DNA recognition with MarR, including backbone flexibility and successive switches of conformation in the presence of hormone.

Biosensor circuits robustly respond to graded concentration of hormones

The yeast *S. cerevisiae* serves a model system and eukaryotic chassis for synthetic biology applications. Furthermore, this organism neither utilizes phytohormones nor involves phytohormone signaling, thereby offering an ideal system for probing coordinated cellular responses to dynamic phytohormone cues. To test putative biosensors in this eukaryotic host, we fused MarR or IacR with a strong herpes simplex virus trans-activation domain (VP64)[24] under the galactose-induced promoter (Fig. 2a,b and Supplementary Fig. 5a). Also, we tagged MarR-type biosensors with mouse ornithine decarboxylase (ODC) degron[25] for fast degradation dynamics. To report circuit response, we used a Green fluorescent reporter (dEGFP) expressed from the synthetic minimal promoter with putative MarR[19] or IacR operator sequences[23], also tagged with uncleavable ubiquitin (G76V mutant)[26] at the N-terminus for fast degradation (Fig. 2a,b and Supplementary Fig. 5a). We found that IacR-VP64 could robustly respond to a stable concentration gradient of IAA with an excellent detection limit towards the nM range (Supplementary Fig. 6a). Similarly, MarR-VP64 responded to the linear SA gradient, however higher SA concentrations (μM range) were effective in the significant reduction of reporter levels (Supplementary Fig. 6b).

To further characterize the dynamics of MarR-type biosensors, we tested the circuit response in a dynamic environment that is governed by transient changes in auxin and SA levels. For that purpose, we developed bench-top customized rapid, cost-effective lithography technologies[27] for the fabrication of microfluidic device (see also Supplementary Fig. 7 and SI for details). This method produces functional microfluidic devices without a need for expensive equipment and cleanroom facilities. The Microfluidics device (Fig. 2b) integrates a time-dependent switching of two independent media inputs, through a chaotic mixer module (Supplementary Fig. 8a,b). To resolve the dynamics of biosensors, we performed a chaotic microfluidic mixing with a linear decrease and subsequent increase of SA and auxin in 10-hour cycles (Fig. 2c,e). We could observe, in our microfluidic experiments, a prominent pulse of reporter gene dEGFP synchronized across the large population of exponentially growing cells

(couple hundred cells per trap) (Fig. 2d,f). These pulses are reminiscent of analogous cycles of charging and discharging of a capacitor (Fig. 2c,e). We speculate that this ’capacitance’ effect is encoded by the structural rigidity of MarR-type repressors observed during ligand binding events (Fig. 1b). Finally, we looked into the precision of circuit response which was defined as relative width of response peak compared to width of hormone input pulse (Fig. 2g). An important trade-off exists such that an increased precision of response will eventually lead to the loss of memory of previous hormone states. We found that both circuits offer > 70% precision, however, IAA biosensor was more precise and showed less delay in response to dynamic hormone input (Fig. 2g).

Taken together, MarR-type biosensors act as biological ’capacitors’ for auxin and SA offering the fairly precise adjustment of a circuit response time to oscillations of hormone levels.

Synthetic phytohormone crosstalk circuit robustly adapts to dynamic changes in the environment

Auxin and SA crosstalk on multiple levels, including transcriptional and posttranslational regulation of plant development and adaptation to the environment[28]. A successful assembly of synthetic orthogonal crosstalk of phytohormones was never been achieved before. Thus, we attempted to combine our auxin and SA biosensor circuits to construct synthetic, orthogonal crosstalk to which we refer as 'CrossTalker' (Fig. 3a). The general scheme of this synthetic module includes the IacR-VP64 activator and MarR repressor directly fused to the repression domain from yeast MIG1 transcriptional regulator[29] (Fig. 3a and Supplementary Fig. 5b). The CrossTalker displayed a robust graded response to step-wise elevations of both phytohormones in multiwell plate fluorescence scanning assays (Fig. 3b). We performed time-lapse microscopy with alternating input conditions for IAA and SA, and we could observe the gated response, reassembling the NIMPLY logic gate (Supplementary Fig. 9a). These results confirm that the synthetic crosstalk device is capable of responding to dynamic concentration gradients.

The reconstitution of *in vivo* hormone gradients in laboratory conditions is far from trivial task. However, our microfluidic platform provides hormone mixing over the time course of the experiment, producing alternating gradients of auxin and SA. For that purpose, we used a double spike generator shifted in phase by π with a period of 10 hours, consistent with the previous experiment. We found that the CrossTalker circuit (Fig. 3a) exhibited dynamic waves of reporter

gene expression (Fig. 3c,d, Supplementary Movie 4). Reporter peaks were separated by approximately three periods of an input signal (Fig. 3e,f) with the negligible variation in peak amplitudes (Supplementary Fig. 9b). To understand the cause of a delay between consecutive response peaks observed in our experiments we constructed a computer model of hormone crosstalk (Supplementary Fig. 10a-c). We found that a model with a delay in the repression pathway (MarR-RD) could produce a similar output (Supplementary Fig. 10c) to that observed experimentally (Fig. 3c).

Thus, these findings from computer model simulations are in good agreement with the observations of delay and less precision (more temporal memory) in MarR response to changes in phytohormone compared to that of IacR circuits (Fig. 2g).

Synthetic crosstalk of hormones adjusts a speed and precision of response to the frequency of external stimulus providing synchronization of cell populations

Next, we tested whether increasing the frequency of stimulus could lead to an increased speed and precision of CrossTalker responsiveness, providing the frequency entrainment mechanism (Fig. 4a). First, we simulated our model with 5-hour repetitive anti-phase pulses of SA and IAA. The computer model simulations of the CrossTalker circuit predict a correct synchronization with the cyclic phytohormone stimulus (Supplementary Fig. 10d). These predictions from the computer model reveal speed and precision of the response change with the frequency of the stimulus, allowing the fast adaptation to the environmental conditions.

Next, we tested this intriguing theory experimentally by subjecting the Crosstalker circuit to 5-hour antithetic pulses of IAA and SA (Fig. 4b). The time-lapse live yeast imaging in microfluidic traps revealed robust, synchronized oscillations of a reporter gene (Fig. 4c, Supplementary Movie 5) with a mean period of 5-6 hours (Fig. 4d) and minimal variation of the amplitude (Supplementary Fig. 11a). Next, we calculated the autocorrelation function of reporter time traces and identified a prominent pattern of synchronized oscillations within a narrow frequency domain (Fig. 4e). Also, we could observe two possible synchronization modes 1:1 and 1.5:1 in our experiments (Supplementary Fig. 11b). Moreover, lab on a chip experiments revealed a dilution of the period of oscillations (phase diffusion) that could potentially impact on the precision of circuit response(Supplementary Fig. 11c). However, the successive increase of

hormone input frequency by the factor of 2 led to faster, sharper and more consistent oscillations (Fig. 4f, Supplementary Movie 6) that were synchronized across different microfluidics traps (Fig. 4g). The autocorrelation analysis of reporter signal dynamics revealed the prevalence of oscillations with shortened periods between 3 to 5 hours (Fig. 4h,i and Supplementary Fig. 11d) compared to those observed with 5h hormone stimulus (Fig. 4d). Minimal or no delay between successive periods indicates a high precision of response (Supplementary Fig. 11e). Finally, we confront the precision of CrossTalker circuit with three different input frequencies. Our data indicate that the faster the changes in the hormone input the faster and more precise response is expected but at the cost of temporal memory loss (Fig. 4j).

Taken together, our findings show that CrossTalker circuit processes dynamic fluctuations in the environment and responds with increased speed and precision by decoding the dominant frequency of the input stimulus. Thus, our minimal crosstalk of hormones generates either temporal memory or high speed precise response that depends on the frequency of hormonal changes.

Discussion

A mechanistic mapping of dynamic environmental inputs into precise outputs is a key to understand design principles underlying phenotype patterns in biology. In plants, phytohormones auxin and SA play pivotal roles in the regulation of growth and immunity, offering plant resilience to different types of environment[1-9]. The absence of direct orthogonal biosensor systems for these and many other hormones hinders the mechanistic understanding of input-output relations[10-15]. We argue that a future generation of phytohormone biosensor systems should offer minimal complexity, structural understanding and ease of portability, such that a minimal regulatory modules can directly implemented in a target host (i.e. plant or plant associated microbes).

Here, we provide an immediate solution to these problems by constructing minimal biosensors for auxin and SA that were derived from bacterial antibiotic resistance proteins [16-21]. By combining structural insights, computer modeling, and microfluidics, we demonstrated our biosensors robustly sense hormone concentration gradients, providing temporal memory or speed and precision depending on the exposure time to hormones. As proof-of-concept synthetic biosensor circuits were tested in the eukaryotic prototype model under the

precisely controlled environment, revealing highly dynamic characteristics. Thus, proposed circuits offer vast opportunities for direct recording of phytohormone distributions across time and space and implementing novel functions such as hormone memory and hormone-driven oscillations. Also, we introduced the concept of synthetic phytohormone crosstalk which offers means for the precise adjustment of both speed and precision of response (on the cost of temporal memory) in relation to the applied frequency of exogenous hormone stimulus. This minimal crosstalk mechanism provides a synchronized responses across cell populations under cyclic hormone perturbations.

Because proposed biosensor circuits are compact and universal that can be directly ported to any prokaryotic or eukaryotic host. Our work offers a solid mechanistic framework for future development of biotechnological innovations in plants, plant associated microorganisms and other eukaryotes. Some applications include direct quantitative high-resolution detection of transient hormone movement and construction of new orthogonal functionalities such as decoding spatio-temporal hormone information into precise response times.

References

1. M. Naseem et al., The nexus between growth and defense signalling: Auxin and cytokinin modulate plant immune response pathways. *Journal of experimental botany* **66** (2015).

2. A. Robert-Seilaniantz, et al., Hormone Crosstalk in Plant Disease and Defense: More Than Just JASMONATE-SALICYLATE Antagonism. *Annual Review of Phytopathology* **49**, 317–343 (2011).

3. M. Lavy & M. Estelle., Mechanisms of auxin signaling. *Development* **143**, 3226–3229 (2016).

4. D. Weijers & D. Wagner., Transcriptional Responses to the Auxin Hormone. *Annual review of plant biology* **67**, 539–574 (2016).

5. D. Kumar., Salicylic acid signaling in disease resistance. *Plant science : an international journal of experimental plant biology* **228**, 127–134 (2014).

6. A. C. Vlot et al., Salicylic Acid, a multifaceted hormone to combat disease. *Annual review of phytopathology* **47**, 177–206 (2009).

7. S. Tan et al., Salicylic Acid Targets Protein Phosphatase 2A to Attenuate Growth in Plants. *Current Biology*, **30** (2020).

8. T. Pasternak et al., Salicylic Acid Affects Root Meristem Patterning via Auxin Distribution in a Concentration-Dependent Manner. *Plant Physiology* **180**, 1725-1739 (2019).

9. M. A. Blazquez et al., Evolution of plant hormone response pathways. *Annual Review of Plant Biology* **71**, (2020).

10. G. Brunoud et al., A novel sensor to map auxin response and distribution at high spatio-temporal resolution. *Nature* **482**, 103–106 (2012).

11. C.-Y. Liao et al., Reporters for sensitive and quantitative measurement of auxin response. *Nature Methods* **12**, 207–210 (2015).

12. W. E. Huang et al., Quantitative *in situ* assay of salicylic acid in tobacco leaves using a genetically modified biosensor strain of *Acinetobacter sp*. ADP1. *The Plant Journal* **46**, 1073–1083 (2006).

13. C. T., Defraia et al., A rapid biosensor-based method for quantification of free and glucose-conjugated salicylic acid. *Plant methods* **4**, 28 (2008).

14. B. Parızkova et al., What Has Been Seen Cannot Be Unseen - Detecting Auxin In Vivo. *International Journal of Molecular Sciences* **18**, 2736 (2017).

15. A. Larrieu et al., Comparison of plant hormone signalling systems. *Essays in Biochemistry* **58**, 165–181 (2015).

16. G. A. Beggs et al., MarR family proteins are important regulators of clinically relevant antibiotic resistance. *Protein science* **29**, 647–653 (2020).

17. S. P. Wilkinson et al., Ligand-responsive transcriptional regulation by members of the MarR family of winged helix proteins. *Current issues in molecular biology* **8**, 51–62 (2006).

18. D. K. Deochand et al., MarR family transcription factors: dynamic variations on a common scaffold. *Critical reviews in biochemistry and molecular biology* **52**, 595–613 (2017).

19. M. N. Alekshun et al., The crystal structure of MarR, a regulator of multiple antibiotic resistance, at 2.3 A resolution. *Nature structural biology* **8**, 710–714 (2001).

20. Z. Hao et al., The multiple antibiotic resistance regulator MarR is a copper sensor in Escherichia coli. *Nature chemical biology* **10**, 21–28 (2014).

21. I. C. Perera et al., MarR homologs with urate-binding signature. *Protein science* **20**, 621–629 (2011).

22. J. C. Scott et al., Functional characterization of the bacterial iac genes for degradation of the plant hormone indole-3-acetic acid. *Journal of chemical ecology* **39**, 942–951 (2013).

23. H.-Y. Shu et al., Transcriptional regulation of the iac locus from Acinetobacter baumannii by the phytohormone indole-3-acetic acid. *Antonie van Leeuwenhoek* **107**, 1237–1247 (2015).

24. K. Seipel et al., Different activation domains stimulate transcription from remote ('enhancer') and proximal ('promoter') positions. *The EMBO Journal* **11**, 4961– 4968 (1992).

25. J. Takeuchi et al., Structural elements of the ubiquitin-independent proteasome degron of ornithine decarboxylase. *Biochemical Journal* **410**, 401– 407 (2008).

26. J. H. Stack et al., A ubiquitin-based tagging system for controlled modulation of protein stability. *Nature Biotechnology* **18**, 1298–1302 (2000).

27. A. Grimes et al., Shrinky-Dink microfluidics: rapid generation of deep and rounded patterns. *Lab on a Chip* **8**, 170–172 (2008).

28. C. S. Westfall et al., *Arabidopsis thaliana* GH3.5 acyl acid amido synthetase mediates metabolic crosstalk in auxin and salicylic acid homeostasis. *Proceedings of the National Academy of Sciences* **113**, (2016).

29. J., Ostling et al., Functional domains in the Mig1 repressor. *Molecular and Cellular Biology* 1**6**, 753 LP – 761 (1996).

30. D. G. Gibson et al., Enzymatic assembly of DNA molecules up to several hundred kilobases. *Nature Methods* **6**, 343–345 (2009).

Acknowledgments: We are grateful to L. Rubio for sharing yeast strain CEN.PK2-1C. Authors thank Mark Estelle for critical discussions at the early stage of the project. This work was supported by the Programa de Atraccion de Talento 2017 (Comunidad de Madrid, 2017-T1/BIO-5654 to K.W.), Severo Ochoa (SO) Programme for Centres of Excellence in R&D from the Agencia Estatal de Investigacion of Spain (grant SEV-2016-0672 (2017-2021) to K.W. via the CBGP). In the frame of SEV-2016-0672 funding M.A. received a PhD fellowship (SEV-2016-0672-18-3: PRE2018-084946) and O.P. is supported with a postdoctoral contract. K.W. was supported by Programa Estatal de Generacion del Conocimiento y Fortalecimiento Cientıfico y Tecnologico del Sistema de I+D+I 2019 (PGC2018-093387-A-I00) from MICIU (to K.W.).

Author contributions: S.P.G and M.G.N designed, performed most of experiments and analyzed data. D.R.S, C.P.N and O.P contributed to plasmid and strain constructions, S.P.G and M.A, performed multi-well plate fluorescence assays. M.G.N performed microfluidics experiments. K.W designed experiments analyzed data and supervised the project. All authors contribute to the manuscript writing.

Competing interests: Authors declare no competing interests.

Data and materials availability: All data that support the findings of this study are available in the manuscript. Original data that supports the findings are available from the corresponding author upon request. Plasmids sequences will be deposited in NCBI database after publication. Correspondence and requests for materials such as should be addressed to K.W. (k.wabnik@upm.es). Image processing and analysis were performed using Fiji (v.1.0) and Matlab (R2018b) and R-studio. Subsequent analysis was performed using custom R and Matlab scripts. The codes are available upon request from the corresponding author.

Methods

Structural modeling and Molecular dynamics simulations

Crystal structures of the apoprotein, DNA-bound and holoprotein were obtained from Protein Data Bank RCSB database (codes: 5h3r, 3voe, and 1jgs). In preparation for MD simulations, structures were process using Charmm-gui (www.charmm-gui.org) Solution Builder. Simulation-ready structures contain hydrogens, water box around the structure fitted to the size of system, and water environment with 0.15M NaCl ions and an isothermal-isobaric (NPT) ensemble with a constant amount of substance (N), pressure (P) and temperature (T). The pressure was set at 1 atm (1.01325 bars) and temperature at 303 K. MD simulations were performed using OpenMM environment (http://openmm.org/) with hydrogen mass repartitioning (HMR) scheme. Initial steps of minimalization and equilibration for 1 ns were followed by tracking 50 ns conformation dynamics with the time step of 2 femtoseconds. Particle Mesh Ewald (PME) periodic boundary conditions were used for the electrostatic force calculations. Trajectory files from the simulations were processed with VMD (www.ks.uiuc.edu/Research/vmd/) to generate RMSD plots and atom distance distributions. The visualization of structures was done in UCSF Chimera (https://www.cgl.ucsf.edu/chimera/). Metadynamics energy landscape analysis was performed in OpenMM using Metadynamics module and Morse/long-distance potential between atomic centroids of R73 (MarR) and K80 (iacR) residues in DB domains. This collective variable (CV) is calculated based on the reference distance of ≈ 20 A$^{\circ}$ inferred from the crystal structure of DNA-bound MarR as en equilibrium

parameter in the Morse potential function. 50ns trajectories were used as a starting point to perform an additional 20ns simulation (total 70ns) with CV in the flexible range of 0-3 nm. The IacR structure models were obtained with Swiss-Model using several templates, RCSB codes: 1jgs, 5hr3 and 3voe .The molecular docking of IacR with two IAA molecules was performed using UCSF Chimera and the AutoDock Vina. IacR and IAA charges were merged and the non-polar hydrogens and lone pairs were removed. In addition, hydrogens were added to the IacR structure. A total of 10 binding modes were generated and best two poses were selected based on the minimal energy score. The exhaustiveness of the search was set to 8.

Structure alignment

Molecular Evolutionary Genetics Analysis (MEGA) was used to produce the alignment of the multiple MarR proteins, specifically the ClustalW program available in MEGA. The Gap Opening Penalty was set at 10.00 and the Gap Extension Penalty at 0.20. The protein weight Matrix used in this multiple alignments was Gonnet. For the visualization and generation of the alignment image, we used the Jalview program with the input alignment file from MEGA.

Strains and plasmid constructions

All plasmids in this study were created using isothermal Gibson assembly cloning[30]. A middle-copy (15-30 copies) episomal plasmid pGADT7 (Takara Bio) was used to increase the concentration of synthetic circuit components in order to buffer for the intrinsic molecular noise. This plasmid was further modified to accommodate three different auxotrophic selection markers (Leucine, Uracil, and Histidine; Supplementary Fig. 5). GAL7 promoter and either CYC1 or ADH1 terminators were cloned and combined with biosensor modules in Activator or repressor plasmids (Supplementary Fig. 5). The reporter plasmids include synthetic minimal promoters with putative MarR or IacR operator sequence upstream TATA-box and fast-degradable UBG76V-EGFP (dEGFP). PCR reactions were performed using Q5 high fidelity polymerase (New England Biolabs). Correct PCR products were digested with DpnI (New England Biolabs) to remove the template and subsequently cleaned up with a DNA cleanup kit (Zymo Research) before Gibson assembly. Constructs were transformed in ultra-competent cells from E. coli DH5a strain using standard protocols. All plasmids were confirmed by colony PCR and validated with sequencing. The CEN.PK2-1C (a kind gift from Dr. Luis Rubio) yeast strain was used to

make competent cells and transformation of plasmids using Frozen-EZ Yeast Transformation II Kit (Zymo Research).

Multiwell plate fluorescence measurements

Overnight culture of the yeast in 2% sucrose low fluorescence media (Formedium, UK) was diluted 100 times and transfer to a 96 well plate with sucrose only or sucrose + galactose conditions and a 2D gradient of phytohormone concentrations. Plates were incubated at 30C overnight in the thermal incubator and well mixed by shaking before performing measurements. Measurements were done with the Thermo ScientificTM VarioskanTM LUX multimode microplate reader. Optical Density was set at an absorbance of 600nm wavelength, the fluorescence excitation and emission light at 488nm and 517nm wavelength, respectively.

Microfluidic Mold fabrication

Molds for the production of microfluidic devices were designed in Adobe Illustrator software and printed on plastic sheets with the monochrome laser printer at 1200dpi resolution. A density of Ink deposition was used to control the feature height. Plastic wafers were cut and transferred to the thermal oven set to 160ºC to shrink by one-third of the original size, the baked again for 10 min to smoothen and harden the ink. Finally, molds were cleaned with soap, rinsed with isopropanol and DDI water and dry using a nitrogen gun and secured with Scotch tape before use.

Soft Lithography

Molds were introduced in plastic 90mm Petri dishes and fixed with double-sided tape. Dowsil Sylgard 184 Polydimethylsiloxane (PDMS) was properly mixed in a 10:1 (w/w) ratio of elastomer and curing agent and stirred until the uniform consistency was achieved. Approximately 27mL of the homogeneous mixture was poured in each petri dish and completely degassed using the 8 CFM 2-stage vacuum pump for approximately 20 minutes. Degassed PDMS was cured at 80ºC for 2h. Cured PDMS was removed from the petri dish, separated from the wafer and cut to extract the individual chips. Fluid access ports were punched with 0.7mm diameter World Precision Instruments (WPI) biopsy puncher and flushed with ethanol to remove

any remaining PDMS. Individual chips were cleaned with ethanol and DDI water and Scotch tape to remove any remaining dirt particles.

Microfluidic device bonding

At least one day before use, individual chips and coverslips were cleaned in the sonic bath and rinsed in ethanol, isopropanol, and water. Both surfaces were exposed to Corona SB plasma treater (ElectroTechnics Model BD-20AC Hand-Held Laboratory Corona Treater) between 45 seconds to 1 minute, then surfaces were brought together and introduce at 80ºC in an oven overnight to obtain the enhanced bond strength.

Calibration of microfluidic mixer module

Mixer Calibration was performed by staining one of two inputs with Rhodamine B 0.001% (w/v). A pair of 60mL syringes were prepared with 20mL of water or water + dye. Three 50mL falcon tubes were filled with 20mL of water and connected to waste and cell loading ports. Syringes and falcon tubes were set on linear actuators which control pressure in the microfluidic device through customized software. The microfluidic device was vacuumed for at least 20 minutes to remove air bubbles and facilitate device wetting before connecting Tygon microbore tubing 0.020” x 0.060”OD (ColePalmer Inc.). After air removal, one syringe was connected and then the other syringes were plugged sequentially once liquid reached and filled the ports. Switching between inputs was regulated with the gravity-aided hydrostatic pressure by changing the relative height of syringes. Increasing height of input media 1 (M1) over input media 2 (M2) produces the pressure difference in the mixing module. Therefore, at maximum height differences, microfluidic chip is filled with 100% of M1 and 0% of M2. Syringe positions were adjusted with 0.1 mm precision by changing height to obtain highly efficient mixing between 0% and 100% . The excessive flow is diverted towards an auxiliary waste output (W1) that releases the pressure from the mixer. Flow then was introduced into the second chaotic mixer to assure a rapid switching of conditions. The calibration process was repeated at least three times with three independent microfluidic devices. Maximum and minimum height settings varied solely by a few millimeters, therefore we used averaged measures without cross-contaminating media inputs, which were following: 610 mm for the maximum and 390 mm for minimum settings, respectively. All three replicates showed exact 50% mixing for the 500 mm settings.

Cell loading procedure

All tubing lines were sterilized with ethanol and plugged to syringes or introduced in falcon tubes under sterile conditions. Fresh yeast colony was grown in low fluorescence media composition (Formedium, UK) with 2% sucrose as a carbon source. The next day, yeast cultures were diluted 10-20 times approximately to 0.2-0.4 $O.D_{600}$ to obtain highly concentrated cells that were transferred to a 50mL falcon tube for loading. 60mL media syringes were filled with 25mL of media with or without hormones and 50mL waste falcons tubes were filled with 10mL of DDI water. Before loading, devices were vacuumed for at least 20 minutes to remove all the air from the channels and traps. Syringes and falcon tubes were placed on the height control system and lines were connected as follows; media syringes were plugged first and kept above all other inputs to prevent media contamination. Adjusting the height of the cells-containing falcon tube as well as media and waste aids in controlling the cell seeding in the traps. Although many cells pass through the chip directly towards the waste port, few cells got captured via micro valves and seeded the traps. Once 10-20 cells were captured in each trapping region, the flow from the cell loading port was reverted by decreasing the height to the same level as for the auxiliary waste.

Time-lapse imaging, growth conditions and data analysis

Live-cell imaging was performed on the Automated inverted Leica DMi8 fluorescence microscope equipped with Hamamatsu Orca Flash V3 camera that was controlled by µManager(micro-manager.org). Images were captured with 40x dry objective NA=0.8 (Leica Inc.).Traps containing cells were imaged every 10 minutes on three different channels (DIC, GFP (Excitation: 488 Emission: 515, and mCherry Excitation: 583, Emission: 610) with CoolLed pE600 LED excitation source and standard Chroma epifluorescent filter set. Experiments were run for up to 72 hours under the continuous supply of nutrients in the microfluidic device. Acquired images were initially processed in Fiji (https://imagej.net/Fiji) using custom scripting to extract positions with exponentially growing yeast cells. Constitutively expressed mCherry marker was used to identify healthy cells that are in the exponential growth phase.

Dead or non-growing individuals were discarded by correcting dEGFP signal according to the formula $dEGFP/(dEGFP + mCherry)$. Each image was divided into 25 regions of interest (ROIs)

and analyzed separately to isolate regions where cells were actively growing and could be tracked over time. The posterior analysis was done with custom R-studio scripts. Firstly, raw data were detrended using the detrend function from "pracma" R package and then smoothed with Savitzky-Golay Smoothing function (savgol), from the same package, with a filter length of 15 was applied and the signal was normalized between 0 and 1 to generate time-course plots and kymographs of traps. Amplitudes were calculated with find peaks within the Process Data using the "findpeaks" function from "pracma" R package with nups and ndowns of 6, and periods were calculated by calculating distances between dEGFP peaks. Precision of response was based on relative differences between peaks widths of stimulus and response, respectively. Precision per *i-th* trap was calculated as follows : $precision^i$ = 1- ($width_output^i$ – *width_input*)/($width_output^i$ + *width_input*). Autocorrelation and power spectrum density per trap were calculated using standard calculations with Matlab derived packages autocorr and Fast Fourier Transformation (fft).

Mathematical modeling

In the CrossTalker model, MarR (*M*) and IacR (*I*) levels as well as dEGFP reporter concentrations (R) were described using Delayed differential equations scheme (DDE) that was implemented in Matlab 2018b Inc. The dde23 DDE function was used to numerically solve for time-dependent concentrations of species. For simplicity, processes such as transcription, translation, and monomer oligomerization were captured in a single parameter (α_o) whereas biosensor degradation was modeled separately as basal(δ_o) and phytohormone- dependent(δ_{sa} and $\underline{\delta_{iaa}}$) rates:

$$\frac{\partial M}{\partial t} = \alpha_o - \delta_o \cdot M - \delta_{sa} \cdot \frac{SA \cdot M^2}{1 + M^2} \tag{1}$$

$$\frac{\partial I}{\partial t} = \alpha_o - \delta_o \cdot I - \delta_{iaa} \cdot \frac{IAA \cdot I^2}{1 + I^2} \tag{2}$$

SA and IAA are normalized salicylic acid and auxin concentrations from 0(min) to 1(max) that follow stimulus pulses (forcing period T_f) according to formulas:

$$SA(t) = 0.5 \cdot (1 + sign(0.5 \cdot \sin(\frac{2 \cdot \pi \cdot t}{T_f}))) \tag{3}$$

and,

$$IAA(t) = 1 - SA(t) \tag{4}$$

The time evolution of reporter gene dEGFP (R) was described as follows:

$$\frac{\partial R}{\partial t} = \frac{\alpha_{Ro} + \alpha_I \cdot \kappa_I \cdot I^2_{\tau_1}}{(1 + \kappa_I \cdot I^2_{\tau_1} + \kappa_M \cdot M^2_{\tau_2})} - \delta_{Ro} \cdot R \tag{5}$$

where α_{Ro} is a leakiness of the promoter, α_I is an IacR-dependent protein production, κ_I is the strength of IacR-dependent activation and κ_M is the strength of MarR-mediated repression. The parameter δ_{Ro} is dEGFP degradation rate. Model integrates two different delays for activation (τ_1) and repression (τ_2), respectively. Model parameters were scanned and predictions qualitatively compared to the experimental time-curse data (Fig. 3b). We found that only an extended delay in repression ($\tau 2 >> \tau 1$) closely mimic these experimental observations (Supplementary Fig. 10c). The same set of parameters was then used for generating Supplementary Fig. 10d with a 50% shorter period of stimulus (Supplementary Table 1).

Supplementary Information contains:

Supplementary Figures 1-11

Supplementary Movies 1-6 legends

Figures

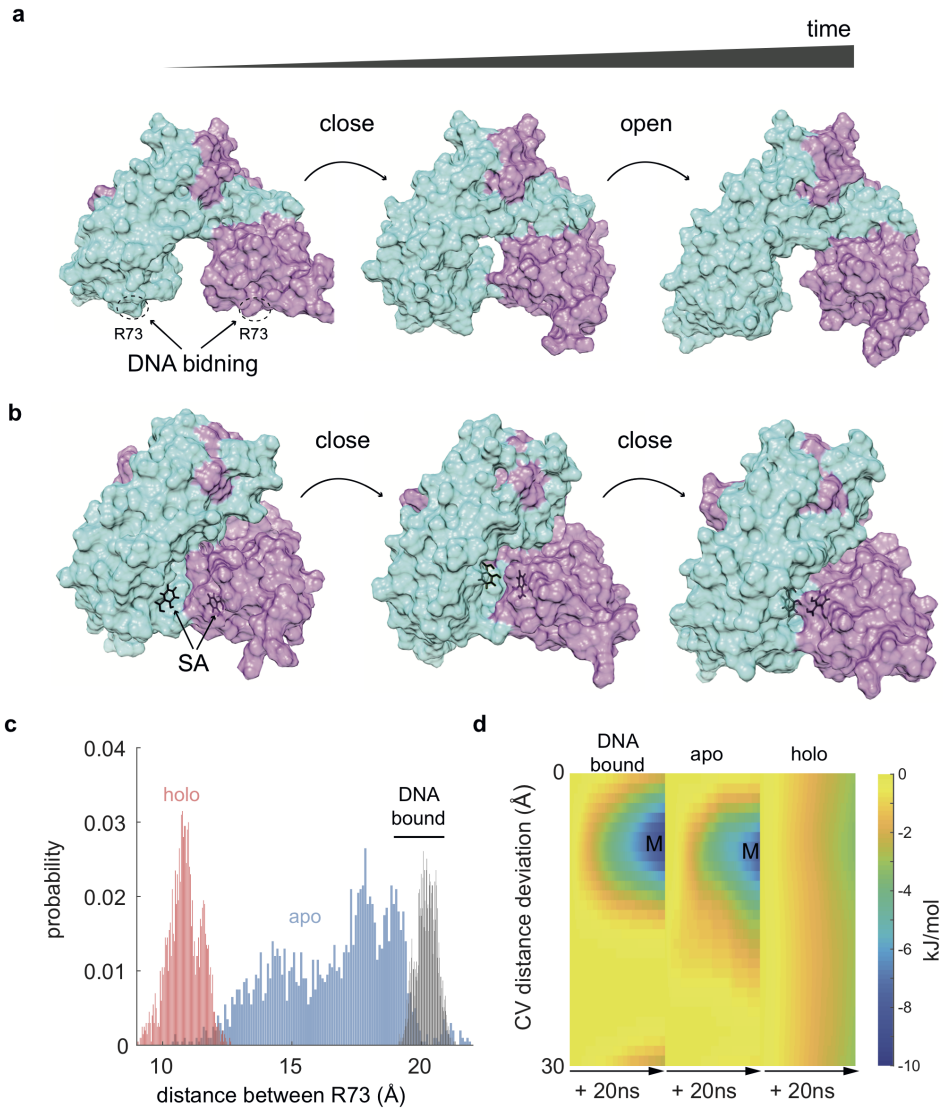
a
time
close
open
R73
R73
DNA bidning
b
close
close
SA
c
0.04
0.03
0.02
0.01
0
probability
holo
apo
DNA bound
10
15
20
distance between R73 (Å)
d
DNA bound
apo
holo
0
30
CV distance deviation (Å)
M
M
+ 20ns
+ 20ns
+ 20ns
0
-2
-4
-6
-8
-10
kJ/mol

Fig. 1. A conformational switch drives the phytohormone sensing through MarR- type regulators.

(**a, b**), Time-lapse from Molecular Dynamics Simulations of the flexible MarR apoprotein (monomers are shown in cyan and purple) (a) (RCSB: 5h3r and 3voe) display a cyclic change of conformation states (open-closed-open). (b), MarR bound to two molecules of SA (black, RCSB: 1jgs) display successive shortening of the distance between R73 that reflects an unbinding of MarR from DNA. (**c**), A probability distribution of the mean distance between R73 atoms of both monomers for apo (blue), holo(red), and DNA-bound (black) configurations. Note that the holo state provides a ≈ 2-fold short distance between DBD domains than that required for a stable bond with DNA. (**d**), Energy landscapes for three MarR configurations (apo, holo, DNA-bound) for deviation from the preferred distance of ≈ 20 A˚between R73 (both chains) required for DNA binding. Note energy minima wells (M) for apo and DNA bound configurations which were absent in holoprotein simulations indicating that the hormone-bound MarR did not reach an energy minimum required for the association with the DNA.

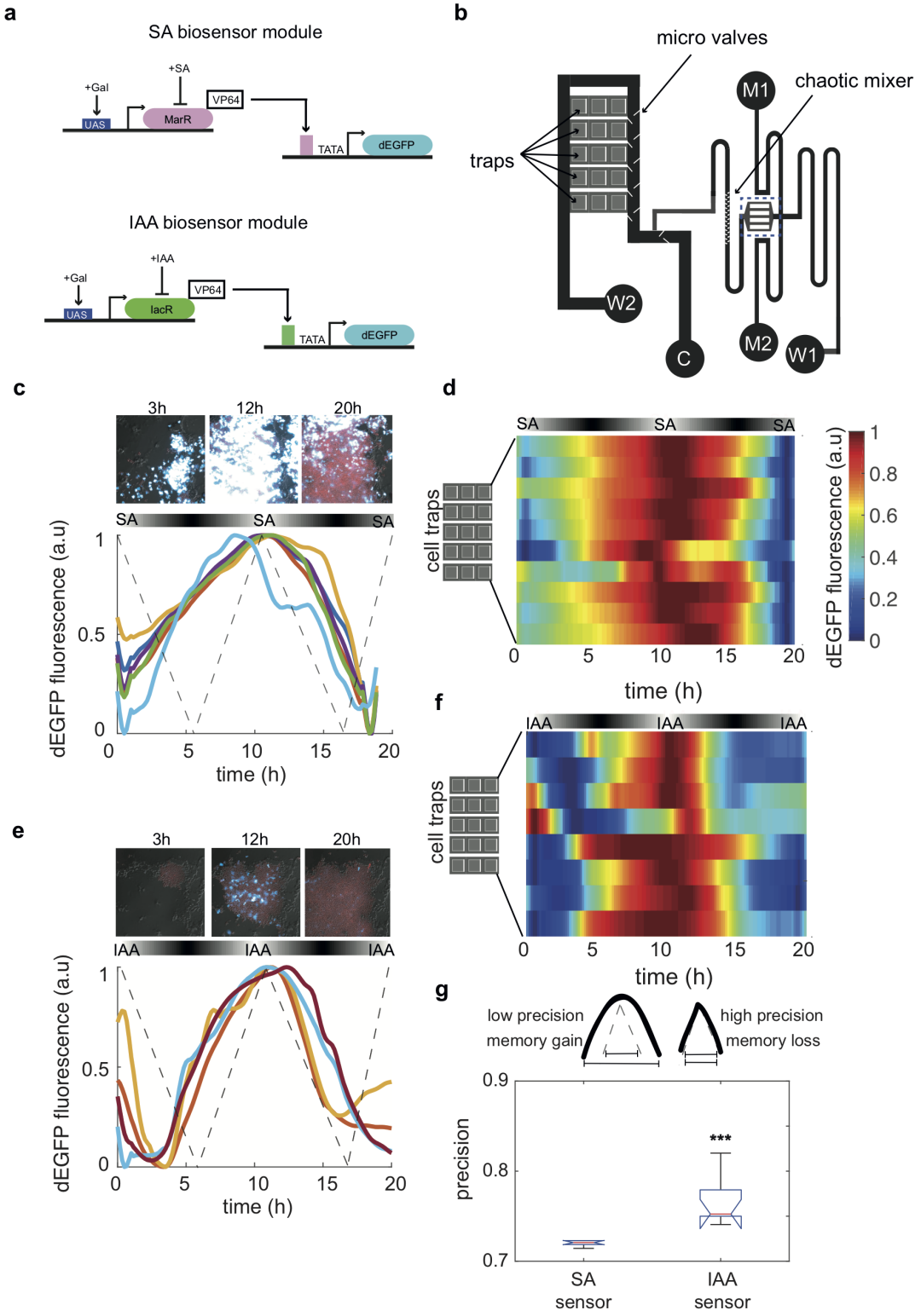
a
SA biosensor module
+Gal
+SA
UAS
MarR
VP64
TATA
dEGFP
IAA biosensor module
+Gal
+IAA
UAS
IacR
VP64
TATA
dEGFP
b
micro valves
chaotic mixer
traps
M1
W2
C
M2
W1
c
3h
12h
20h
SA
SA
SA
dEGFP fluorescence (a.u)
time (h)
d
SA
SA
SA
cell traps
dEGFP fluorescence (a.u)
time (h)
e
3h
12h
20h
IAA
IAA
IAA
dEGFP fluorescence (a.u)
time (h)
f
IAA
IAA
IAA
cell traps
time (h)
g
low precision
memory gain
high precision
memory loss
precision
***
SA
sensor
IAA
sensor

Fig. 2. Biosensor circuits show a high dynamic range in response to linear concentration gradients of phytohormones.

(**a**), Schematics of SA (a) and IAA (b) biosensor circuits. MarR or IacR repressors are tagged with a synthetic VP64 viral transactivation domain, nuclear localization signal (NLS), and ODC degron. Galactose is used to induce the transcription of biosensors. The fluorescent reporter (dEGFP) contains an uncleavable ubiquitin (G76V) tagged to N-terminus of enhanced GFP (EGFP) that is driven by the minimal promoter with either MarR(pink bar) or IacR(green bar) operators placed directly upstream of TATA-box. (b), Schematics of microfluidic device used in this study. M1 and M2 are media ports with chaotic and static mixers of hormones. W1 and W2 are main waste outputs and C is cell loading port. Single cells are captured at C and grow into large colonies of hundreds cells in the trapping module. (**c-f**), Examples of screenshots, time traces (c, e) and heat maps (d,f) across different traps from independent microfluidic experiments with linear changes of phytohormones (dashed lines). Three channels were merged Differential interference contrast (DIC), normalized dEGFP (cyan), and mCherry (marker for exponentially growing cells). Cells transformed with MarR biosensor circuit (c, d) displayed a broader peak and slower response to a cyclic linear change in hormone concentrations (10 hours period of SA or IAA) compared to cells equipped with the synthetic IAA sensor (e, f). **(g),** Precision of response was determined by relative difference between response and stimulus peak widths. Circuit precision is inversely correlated with a temporal memory or 'capacitance' of previous hormone state. Comparison of precision between both biosensors calculated for at least n=10 independent traps per biosensor using one-way ANOVA test ($p < 0.001$).

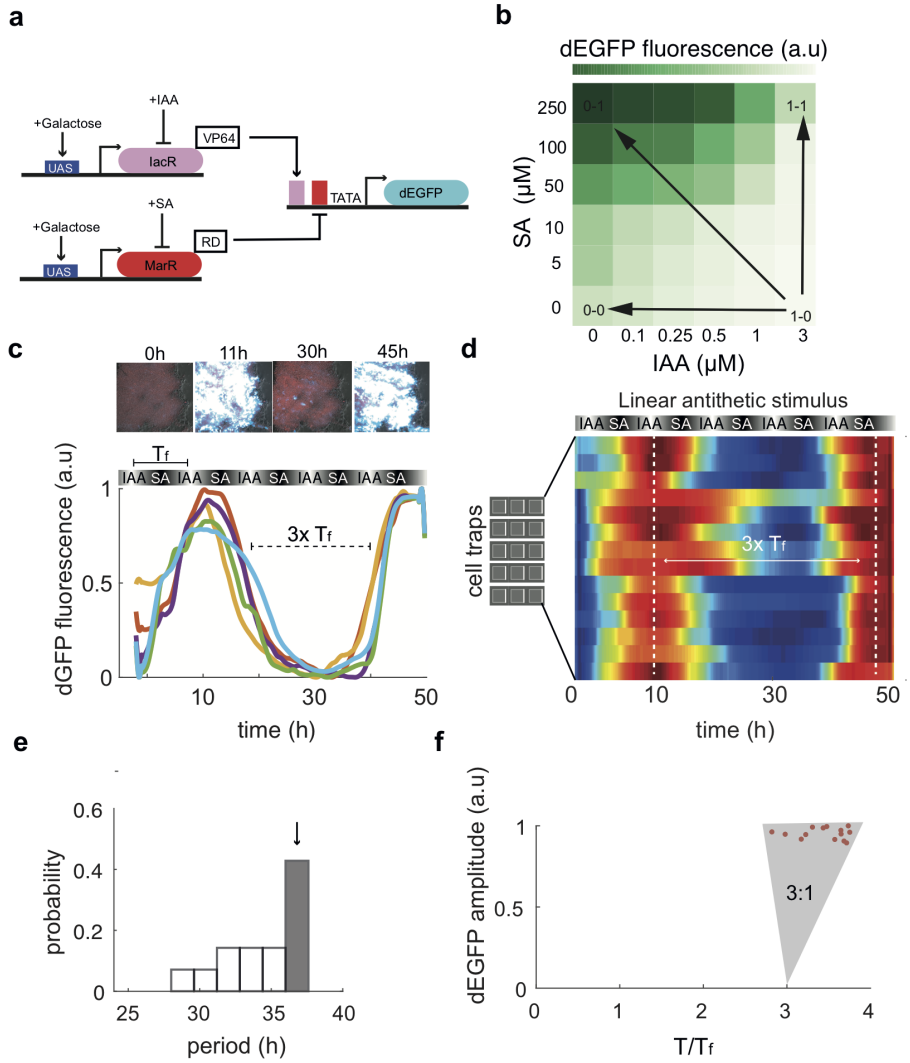
a
+Galactose
UAS
+IAA
IacR
VP64
TATA
dEGFP
+Galactose
UAS
+SA
MarR
RD
b
dEGFP fluorescence (a.u)
SA (μM)
250
100
50
10
5
0
0-1
1-1
0-0
1-0
0
0.1
0.25
0.5
1
3
IAA (μM)
c
0h
11h
30h
45h
Tf
IAA SA IAA SA IAA SA IAA SA IAA SA
3x Tf
dGFP fluorescence (a.u)
1
0.5
0
10
30
50
time (h)
d
Linear antithetic stimulus
IAA SA IAA SA IAA SA IAA SA IAA SA
cell traps
3x Tf
0
10
30
50
time (h)
e
probability
0.6
0.4
0.2
0
25
30
35
40
period (h)
f
dEGFP amplitude (a.u)
1
0.5
0
3:1
0
1
2
3
4
T/Tf

Fig. 3. CrossTalker circuit responds to linear gradients and dynamic alterations of both hormones on the microfluidic chip and fluorescence assays.

(**a**), Implementation of the CrossTalker circuit. MarR was tagged with the repression domain consisting of the last 24 amino acids of MIG1 transcriptional repressor, nuclear localization signal (NLS), and mouse ODC degron and combined with activating IacR-VP64-ODC construct. A synthetic promoter that drives dEGFP, consists of IacR and MarR operators upstream of TATA-box. **(b)**, Dual gradient scans on CrossTalker reveals four boundary states (0-0; 1-0;0-1; 1-1) reminiscent of the NIMPLY logic gate (average of triplicates is shown). Fluorescence was normalized to OD_{600} as described in Supplementary Fig. 6. (**c, d**), Examples of CrossTalker circuit dynamics in cells that were grown in the microfluidic device with 10-hour antithetic waves of SA and IAA consistent synchronized across 14 independent trapping regions was observed (d). (**e**), A histogram of mean period distribution from 14 traps on the microfluidics chip. Gray bar show a dominant frequency of response. (**f**), The plot of mean dEGFP fluorescence amplitude against the ratio of response (T) and input forcing (T_f)) periods in 14 independent traps. The shaded synchronization region; 3 periods of stimulus corresponds to a single period of CrossTalker circuit response.

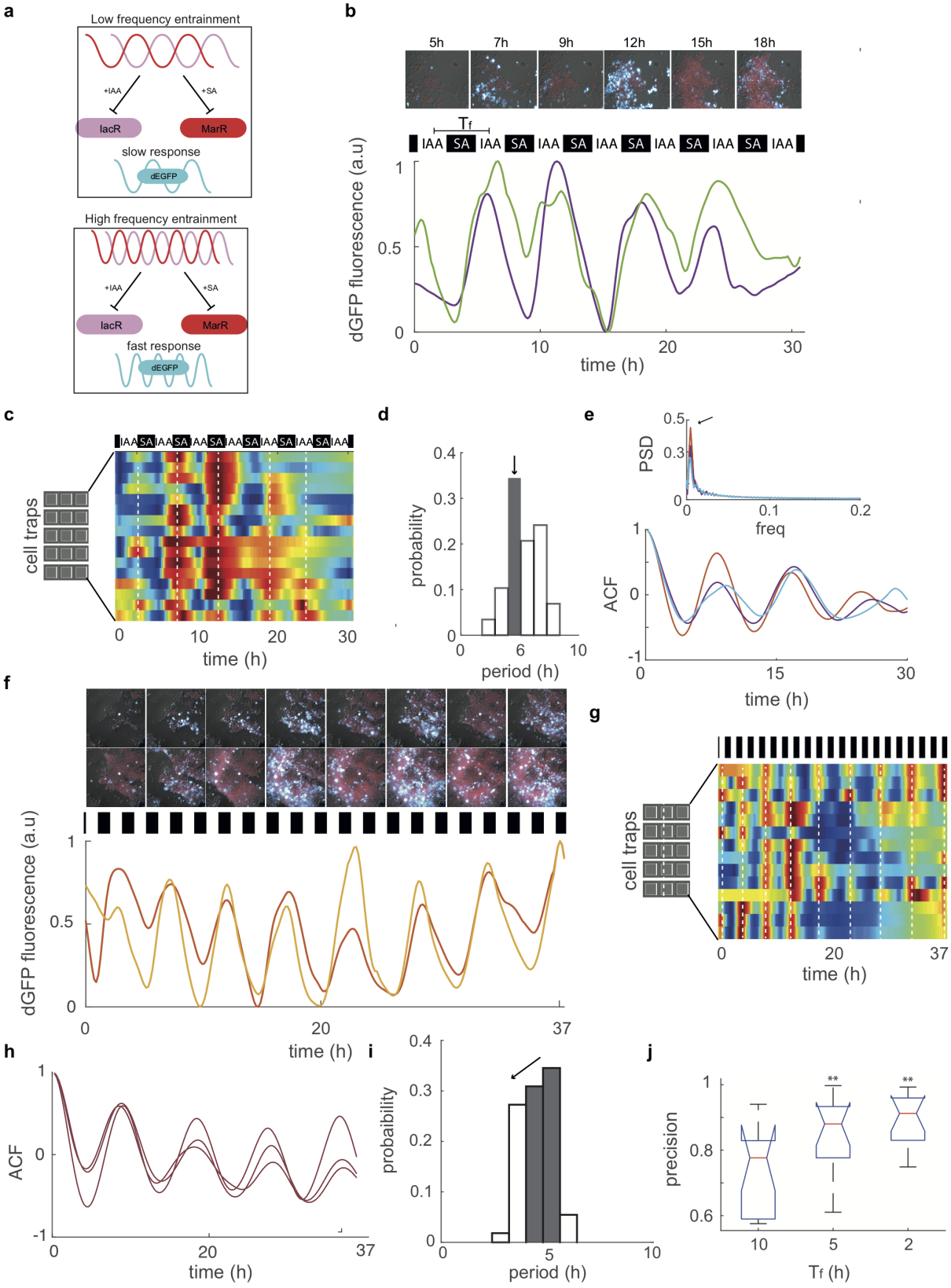
a
Low frequency entrainment
+IAA
+SA
lacR
MarR
slow response
dEGFP
High frequency entrainment
+IAA
+SA
lacR
MarR
fast response
dEGFP
b
5h
7h
9h
12h
15h
18h
Tf
IAA SA IAA SA IAA SA IAA SA IAA SA IAA SA IAA
dGFP fluorescence (a.u)
time (h)
c
IAA SA IAA SA IAA SA IAA SA IAA SA IAA SA IAA
cell traps
time (h)
d
probability
period (h)
e
PSD
freq
ACF
time (h)
f
dGFP fluorescence (a.u)
time (h)
g
cell traps
time (h)
h
ACF
time (h)
i
probaibility
period (h)
j
precision
Tf (h)

Fig. 4. CrossTalker circuit synchronizes cell populations with the dynamic hormone input through the frequency-entrainment mechanism.

(**a**), A cartoon demonstrates the principles of frequency entrainment mechanism for the Crosstalker circuit. For slow cycles of the input stimulus, a circuit displays a slow response (upper panel). Increased frequency of the stimulus is decoded by the circuit to adjust the speed of response (lower panel). (**b, c**), Dynamics of crosstalk circuit response towards the 5h antithetic hormone pulses (b) show a fair synchronization across traps 16 traps (c), revealing input frequency-dependent tunability of the CrossTalker circuit. (**d**), A period probability distribution displays a dominant frequency (gray bar) of response locked to the input signal frequency. (**e**), Autocorrelation (ACF) (lower panel) and power spectrum density functions (PSD)(top panel) across different traps demonstrate a periodic character of circuit response with a dominant frequency peak (top panel). (**f**), Image snapshots (every 2h) and time traces of circuit oscillations with rapid 2-hour antithetic hormone pulses. (**g**), Improved synchrony across cell populations shown in 14 traps in the microfluidic chip. (**h**), cumulative ACF plots for example traps show a sustained periodic pattern. (**i**), A period probability distribution displays frequency shift to the lower periods (gray bars, arrow). (**j**), Comparison of circuit precision for three different frequencies of hormone input. Precision, speed increased with the frequency of applied input on the account of memory loss. Comparison of precision between both biosensors calculated for at least n=14 independent traps per biosensor using one-way ANOVA test ($p < 0.01$).